JGR Oceans

RESEARCH ARTICLE
10.1029/2022JC018879

Ocean Variability Beneath the Filchner-Ronne Ice Shelf Inferred From Basal Melt Rate Time Series

Irena Vaňková[1,2] **and Keith W. Nicholls**[1]

[1]British Antarctic Survey, Natural Environment Research Council, Cambridge, UK, [2]Now at: Los Alamos National Laboratory, Los Alamos, NM, USA

Key Points:

- Melt rate time series from Filchner-Ronne Ice Shelf show multiple time scales of variability with a character that varies spatially
- Inter-annual melt rate variations driven by sea-ice concentration anomalies are limited to a pathway through the central Ronne Ice Shelf
- Existing melt rate estimates from satellite data dramatically overestimate the amplitude of inter-annual melt rate variability

Correspondence to:
I. Vaňková,
vankova@lanl.gov

Citation:
Vaňková, I., & Nicholls, K. W. (2022). Ocean variability beneath the Filchner-Ronne Ice Shelf inferred from basal melt rate time series. *Journal of Geophysical Research: Oceans*, *127*, e2022JC018879. https://doi.org/10.1029/2022JC018879

Received 19 MAY 2022
Accepted 24 SEP 2022

Abstract Fourteen phase-sensitive radars (ApRES) were deployed on the Filchner-Ronne Ice Shelf (FRIS) to measure variability in its basal melt rate. Melt rates from sites along the Ronne Depression vary seasonally, consistent with the dynamics of the propagation of seasonal dense water from the western ice front into the cavity. Several sites at the back of the FRIS cavity feature a signal with two seasonal maxima. Sub-ice shelf oceanographic data available from one of the sites indicate that this signal is caused by two different pathways followed by the same source water. Inter-annual variability is strongest along a direct flow pathway between western Ronne Ice Front and western Berkner Island. Highest melting occurred in 1999 and 2018, following anomalously low summer sea-ice concentrations in front of the ice shelf. Inter-annual melt rate variability at the back of the FRIS cavity is limited. If present, it is expressed as a suppression or delay in the arrival of the seasonal melt rate minimum, which can be understood in terms of inter-annual stratification changes and variable inflow pathways toward the sites. Long term mean ApRES melt rates agree with estimates from satellite data over eastern FRIS. However, the satellite estimates overstate the area of active basal freezing in the western part of the ice shelf. Furthermore, the temporal melt rate variability from the satellite estimates exaggerates the range of variability at both seasonal and inter-annual time scales with any correspondence between the in-situ and remotely derived inter-annual variability being limited to a single site.

Plain Language Summary Ice shelves form the floating extension of the Antarctic Ice Sheet and they are melted at their base by the ocean beneath. Changes in the rate of ice-shelf melting can affect the ice-shelf thickness and impact the flow of the grounded ice sheet. Melt rate changes also modify the properties of waters exported to the surrounding ocean. We used multiple ground-based, downward-looking radars to monitor the rate of basal melting across the Filchner-Ronne Ice Shelf (FRIS), the most voluminous ice shelf in Antarctica. We used the basal melt rate time series together with previously acquired ocean data from beneath the ice shelf to infer and understand seasonal and inter-annual oceanic variability beneath FRIS and to describe its spatial differences across this extensive ice shelf. Additionally, we compared the in-situ melt rate measurements with estimates from satellite data, concluding that the satellite-derived melt rates significantly overestimate the range of temporal variability experienced at FRIS.

1. Introduction

Where the Antarctic Ice Sheet goes afloat it forms ice shelves that extend into the ocean and interact with it. Ice shelves play an important role in Earth's climate. They buttress the grounded ice, and they modify the ocean properties by cooling and freshening water masses in their underlying ocean cavities. Ice-shelf cavities are difficult to access and monitor directly, and thus our knowledge of sub-ice shelf oceanic variability, which is capable of driving the evolution of the ice sheet, remains limited. A useful quantity that encompasses the interaction of ocean waters with the ice-shelf base and one that can be estimated from the ice-shelf surface is the basal melt rate. Basal melt rate variability is caused by variability in ocean properties in the cavity. Therefore, useful information about ocean dynamics in the cavity may be inferred from melt rate measurements. Here we investigate ocean variability beneath the Filchner-Ronne Ice Shelf (FRIS) using new basal melt rate time series combined with existing ocean mooring data.

Situated in West Antarctica, FRIS extends over the southern portion of the Weddell Sea continental shelf (Figure 1). Year-round freezing temperatures and predominantly southerly winds ensure that the continental shelf is a site of intense sea-ice formation. Sea ice is moved northwestward by the winds that keep the shore lead at the ice front sea-ice free and able to form more sea ice that is immediately exported (Nicholls et al., 2009). Brine

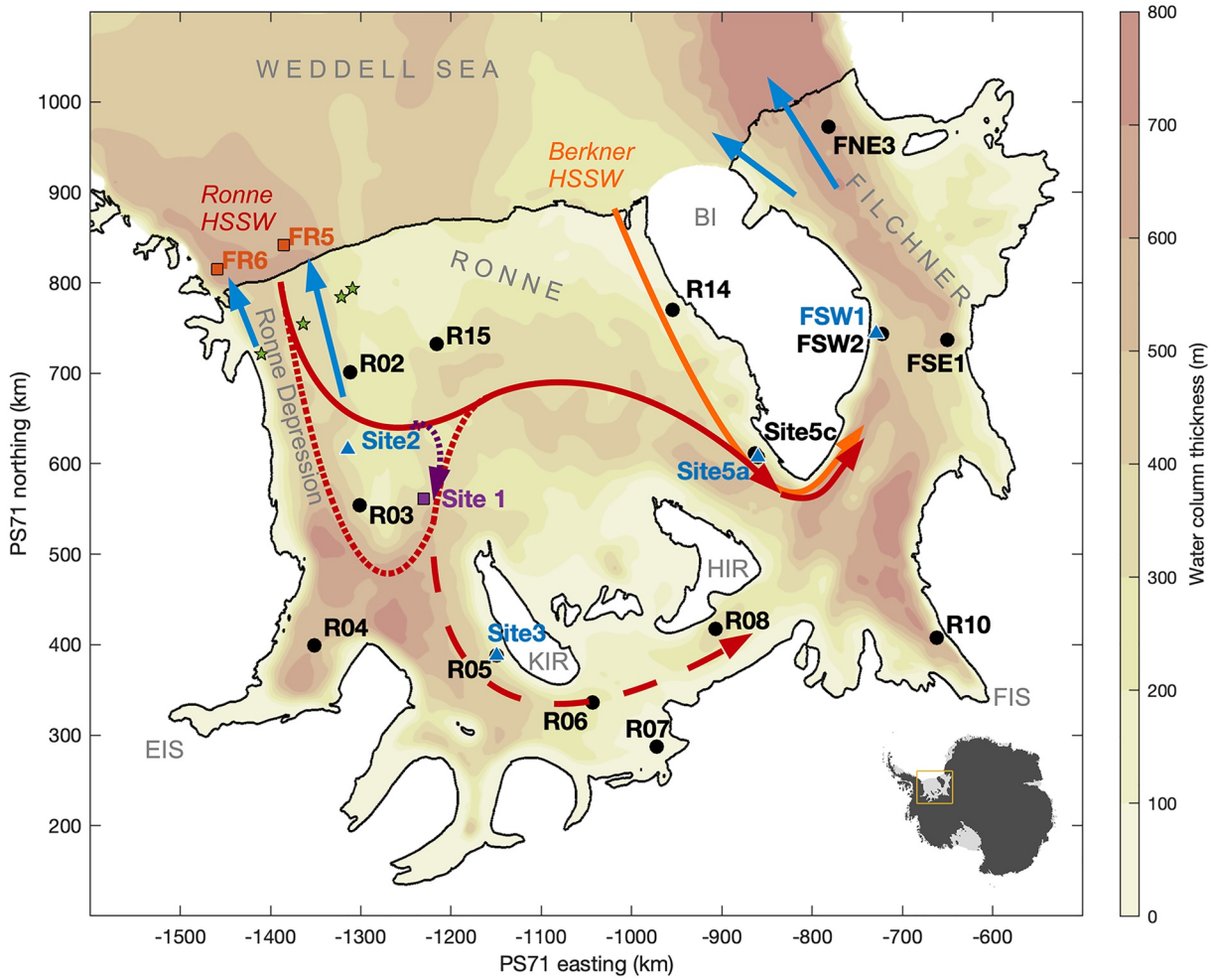

Figure 1. Map of the Filchner-Ronne Ice Shelf using the polar stereographic projection (PS71), inset shows study area location in Antarctica. The contours mark water column thickness in 100-m intervals, the colormap being saturated at 800 m. The deployment sites include ApRES (black dots), sub-ice shelf moorings (blue triangles for time series shown here, green stars for mooring array, i.e., referenced in Section 4.3, and purple square for Site 1 referenced in Section 5.1), and ocean moorings (red squares). Geographic labels are as follows: EIS = Evans Ice Stream, FIS = Foundation Ice Stream, KIR = Korff Ice Rise, HIR = Henry Ice Rise, BI = Berkner Island. Flow pathways are shown schematically. Ronne and Berkner High-Salinity Shelf Water (HSSW) inflows are in red and orange, respectively. Blue arrows mark known Ice-Shelf Water outflows. Our results show that the inter-annual variability in the Ronne HSSW volume propagates across the center of the Ronne Ice Shelf (the solid and possibly also the dotted line), but the signal doesn't reach the back of the cavity behind KIR and HIR (the dashed line). Dotted purple line indicates a plausible inter-annual alternative of faster flow toward R05.

rejection during sea-ice formation produces High-Salinity Shelf Water (HSSW). Although Modified Weddell Deep Water (MWDW), which is warmer than HSSW, penetrates beneath the central Ronne Ice Front, it does not reach deep inside the FRIS cavity. HSSW is thus the warmest and densest water mass reaching the FRIS grounding lines, flushing the cavity and driving its circulation. The HSSW temperature is fixed to the surface freezing temperature (−1.9 C) but as it descends into the depths of the cavity it is able to melt ice, because the freezing point decreases with increasing pressure. By interacting with the ice-shelf base HSSW is transformed into Ice-Shelf Water (ISW), a potentially supercooled water mass that fills most of the cavity. ISW that becomes sufficiently light to escape the cavity and the continental shelf constitutes the coldest water mass contributing to Antarctic Bottom Water (Nicholls et al., 2009).

Two flavors of HSSW are present along the Ronne Ice Front, the denser Ronne HSSW in the west and the lighter Berkner HSSW in the east (Foldvik et al. (1985), Figure 1). The waters that constitute the Ronne HSSW are formed over the south-western continental shelf and gathered at its deepest bathymetric location, the Ronne Depression (Figure 1). The time elapsed since the last contact with the atmosphere for the densest waters in the depression is five years (Janout et al., 2021). The resulting west-east pressure gradient, set by the water mass distribution along

the ice-shelf front, is what drives flow through the FRIS cavity. The dense HSSW descends into the cavity as a gravity current following the southward sloping continental shelf and, under the influence of rotation, it hugs the eastern flank of the depression (Jenkins et al., 2004; Nicholls & Makinson, 1998). Part of the inflowing HSSW is routed southeastward via a bathymetric deepening north of Site 2 (Nicholls & Østerhus, 2004), across the central Ronne Ice Shelf toward Site 5, near Berkner Island (solid red line in Figure 1). The remainder continues to the back of the cavity passing by Site 3 (Nicholls et al., 1997), west of Korff Ice Rise (dotted and then dashed red line in Figure 1). Two distinct ISW outflows from beneath the Filchner Ice Shelf have been linked to these two pathways, with the corresponding outflows being two, respectively six years older than their source water, the Ronne HSSW (Janout et al., 2021). Berkner HSSW also enters the cavity, west of Berkner Island and it has been observed at the upper part of the water column at Site 5 (Nicholls et al., 2001). Berkner HSSW drives flow counter clockwise around Berkner Island (orange solid line in Figure 1) and eventually contributes to the west most ISW outflow from beneath the Filchner Ice Shelf.

Much of the present understanding of how the variability in HSSW production impacts circulation beneath FRIS has been established using observations from Site 2, Site 3, and Site 5 (Figure 1) during different periods between 1992 and 2003 (Nicholls, 1996; Nicholls, 1997; Nicholls & Østerhus, 2004). At depth, Site 2 and Site 3 are dominated by a seasonally varying thickness of HSSW (Nicholls, 1997) that propagates from the western Ronne Ice Front, driven by seasonal convection over the continental shelf. These sites along the eastern flank of the Ronne Depression showed only weak inter-annual variability (Nicholls & Østerhus, 2004). Site 5 (Figure 1) was occupied in the austral summer of 1998/1999 following anomalously high sea-ice production during the autumn of 1998 from an unusually extensive Ronne shore lead during summer 1997/1998 (Ackley et al., 2001; Hunke & Ackley, 2001). The propagation of the related HSSW anomaly was captured at Site 5, and the strong inter-annual variability observed there, compared with primarily seasonal variability at Site 2 and Site 3, led Nicholls and Østerhus (2004) to conclude that the HSSW volume inside the southern portion of the Ronne Depression is largely capped by the bathymetric deepening north of Site 2 and any excess HSSW volume follows the central Ronne Ice Shelf pathway (Figure 1).

Following the modeling study of Hellmer et al. (2012) that proposed the possibility of warm deep water inflow into FRIS via the Filchner Trough under a projected change in sea-ice concentration and wind forcing, further observational attention has turned to Filchner Ice Shelf. There, Hattermann et al. (2021) observed significant inter-annual variations in sub-ice shelf water properties near the Filchner Ice Front, including intermittent intrusions of Berkner HSSW beneath the ice shelf. These dynamics were again related to changes in the circulation strength beneath FRIS that are set by the HSSW forcing originating over the continental shelf north of the Ronne Ice Front (Hattermann et al., 2021; Janout et al., 2021).

Antarctic-wide maps of mean melt-rate estimates can be constructed from satellite data (Rignot et al., 2013), however, detecting melt rate variability using this technique is challenging; although quarter-yearly estimates are now available (Adusumilli et al., 2020), they have not been validated. The need to measure basal melt rate variability at oceanographic time scales drove the development of a phase-sensitive radar (ApRES), which samples autonomously from the ice-shelf surface and provides precise measurements of ice-shelf melt-induced thickness changes (Brennan et al., 2014; Nicholls et al., 2015). This technique has been used at a number of ice shelves and ice tongues to detect variability at timescales ranging from tidal and diurnal to weekly, fortnightly, and seasonal (Nicholls, 2018; Davis et al., 2018; Lindbäck et al., 2019; Sun et al., 2019; Vaňková et al., 2020; Washam et al., 2019).

Here, we use 14 ApRES instruments deployed across FRIS (Figure 1) to characterize primarily its seasonal and inter-annual melt rate variability. Where available, melt rate estimates are extended to the past by applying a validated melt rate parameterization to previously acquired ocean observations in the cavity. The resulting melt rate time series are used to validate, update or revise past hypotheses formulated based on more spatially and temporally limited observations.

This paper is structured as follows. Section 2 describes the datasets in this study and the methods used to construct multiyear melt rate time series. ApRES melt rate time series are presented in Section 3. Seasonal and inter-annual melt rate variability is analyzed in Sections 4 and 5, respectively. Comparison of the in-situ melt rate estimates with estimates from satellite data are presented in Section 6. Section 7 summarizes our conclusions.

2. Data and Methods

2.1. Data

Basal melt rate time series were derived from several ApRES instruments that collected year-round data from FRIS. The time series vary in length from a few months to six years; the locations are shown in Figure 1 and the extent of the time series can be seen from Figure 2. Parts of this data set have been used previously to characterize semidiurnal tidal melt rate variability (Vaňková et al., 2020), intermittent basal freezing (Vaňková, Nicholls, & Corr, 2021), and melting at specific areas of interest, such as at Site 5 (Nicholls, 2018) and near the Filchner Ice Front (Hattermann et al., 2021). Here we present the complete dataset up to the beginning of year 2022 and focus on characterizing seasonal and inter-annual variability at sites where the record is sufficiently long. Most sites sampled at 2-hr intervals, with the exception of Site 5c, which sampled hourly. Because of power issues, sampling frequency was reduced to seven days for R10 upon servicing in January 2017 and to five days for R07 in April 2020.

In addition to the ApRES data, we also make use of existing ocean data from sub-ice shelf moorings. These include previously published data from Site 2 (Nicholls, 1996), Site 3 (Nicholls, 1997), Site 5 (Nicholls & Østerhus, 2004; Nicholls, 2018; Hattermann et al., 2021), and FSW1 (Hattermann et al., 2021). From these moorings the following measured quantities are used in this paper. From Site 2 we use temperature measurements from thermistors at distances of 108, 213, and 283 m from the ice base. From Site 3 we use temperature time series from five locations, 21, 89, 177, 266, and 389 m below the ice base, and velocity data from 389 m below the base. Also from Site 3 we use thermistor cable data from within 20 m of the ice-shelf base, with individual temperature sensors spaced at 2–4 m intervals. The historic Site 3 mooring and thermistors are collocated with ApRES site R05 (Figure 1), for simplicity, hereafter we will refer to both Site 3 and R05 as R05. Site 5 consists of two deployment sites, Site 5a and Site 5c, that are located within 5 km of each other. Site 5a was instrumented with a mooring between 1999 and 2003 and then with an ApRES starting in 2019. Site 5c has a year-long ApRES record covering 2015 and ocean mooring data between 2015 and 2020. From the Site 5c mooring we use temperatures measured at 20, 38, 84, and 155 m from the ice base and velocity measurements from 20 and 155 m distances. From the Site 5a mooring we use the temperature and velocity data at 84 m from the base. From FSW1 we use temperature, salinity and velocity measurements from instruments located 70 and 410 m below the ice base.

2.2. ApRES Melt Rates

ApRES detects and monitors through time the position of internal and basal reflectors in a Lagrangian frame of reference. Precise detection of changes in the reflector positions is enabled by measuring the phase of the reflected signal (Brennan et al., 2014). At each time step ApRES provides a range profile of amplitude and phase of the returned signal. This complex signal is then cross-correlated for each pair of consecutive time shots to derive vertical displacement time series for internal and basal reflectors (Stewart, 2018; Vaňková et al., 2020). To derive a basal melt rate, we first estimate internal ice dynamics and near surface processes by inspecting displacements of internal reflections following Nicholls et al. (2015) and we subtract those from the time-series of total thickness evolution, which is then differentiated with respect to time. The resulting melt rate time series were low-pass filtered with a 1.5-day Butterworth filter to remove diurnal and semidiurnal tidal variability. The focus of this paper is on seasonal and inter-annual timescales of variability and these are highlighted using a 30-day low-pass filter, which removes, among other features, the relatively strong fortnightly melt rate variations generated by spring-neap tide.

2.3. Melt Rate Parameterization

Contemporaneous measurements of basal melt rates and ocean properties near the ice base can be used to calibrate a melt rate parameterization for a given location on an ice shelf. This allows us to extend the basal melt rate time series to periods when only ocean data were available. Jenkins et al. (2010) showed that the following melt rate parameterization is appropriate for mean melt rates at R05:

$$\dot{m}\rho_i L_i = \rho_i c_i \kappa_i \left.\frac{\partial T_i}{\partial z}\right|_b - \rho_w c_w U C_d \Gamma_{TS}(T_f - T_w)\,, \tag{1}$$

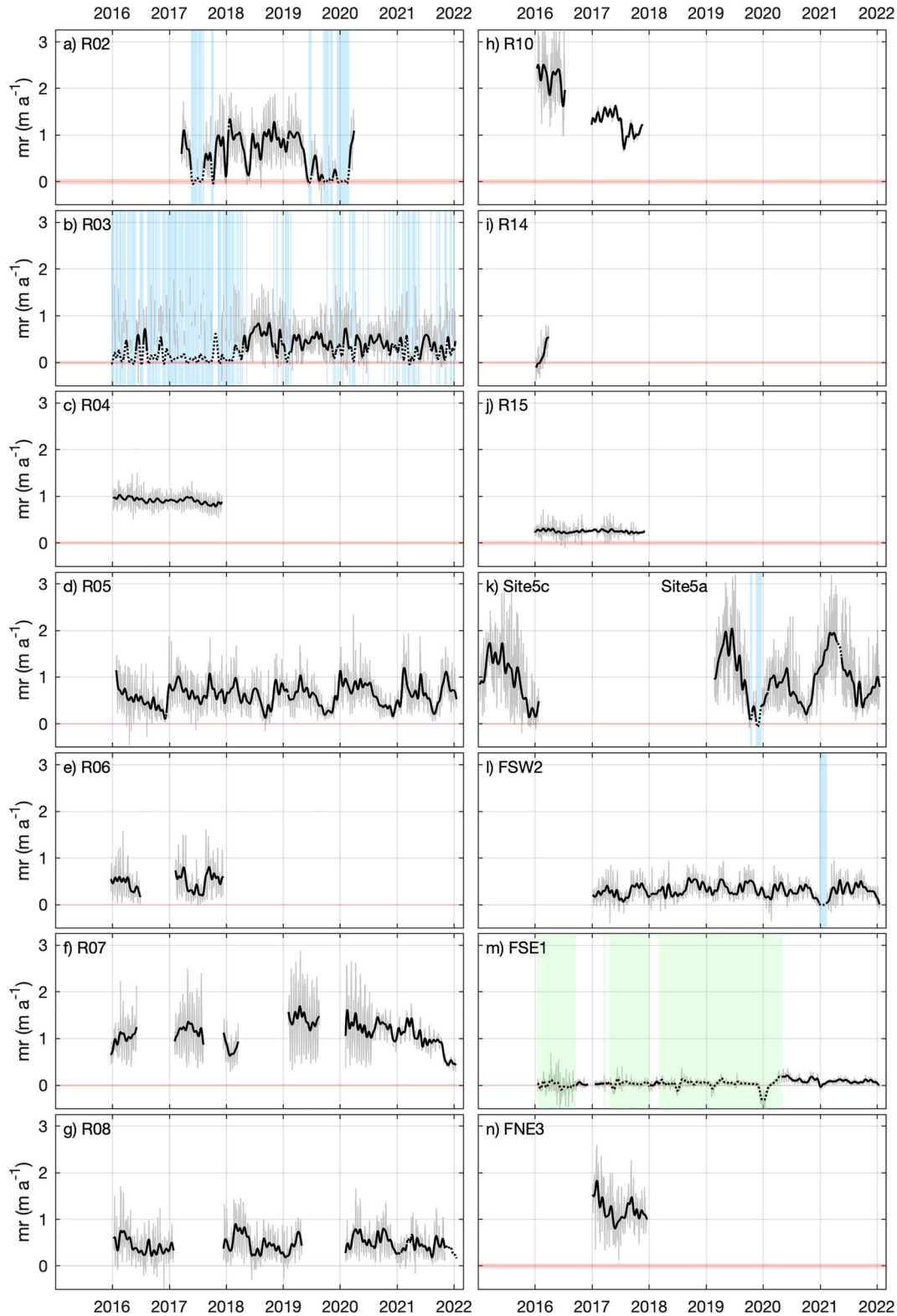

Figure 2. Basal melt rate time series derived from ApRES. In gray are melt rates filtered using 1.5-day low-pass filter and in black using 30-day low-pass filter. Formal uncertainty in the mean melt rate is visualized as a red shading around zero melt rate. Blue shading marks events when ice was accreted at the ice base as a result of basal freezing. Green shading over FSE1 marks periods when the ice base was at or near basal freezing, and where the high-frequency melt rate variability is unreliable. The 30-day low-pass filtered time series is dotted over data gaps, poor quality data, and accreted ice events.

where $\dot{m}$ is the melt rate, L the latent heat of fusion, ρ the density, c the specific heat capacity, κ the thermal diffusivity, T the temperature and U the free-stream flow speed; the subscripts i, w, b and f refer to ice, water, ice-ocean boundary, and the freezing point, respectively. The unique tunable parameter in this formulation is the Stanton number, $C_d\Gamma_{TS}$. Nicholls (2018) successfully used this parameterization for contemporaneous ocean and basal melt rate data from Site 5c, showing that the same $C_d\Gamma_{TS}$ applied across different timescales from annual mean down to diurnal. Here we use the same approach to calibrate $C_d\Gamma_{TS}$ and extend basal melt rate time series for R05 and Site 5.

2.3.1. R05

The water column beneath R05 was occupied with moored instruments in 1996 (Nicholls et al., 1997), including a number of thermistors near the ice-shelf base that recorded to the end of 2004, yielding nine years of temperature measurements. An annual mean melt rate was obtained from repeat phase sensitive radar measurements (Jenkins et al., 2010), allowing the calibration of $C_d\Gamma_{TS}$ at this location. To estimate a long-term melt rate evolution at R05, we assume the parameterization is valid for all timescales of interest and apply it to the full nine-year long thermistor record. This is done after correcting for a small drift in the thermistor time series caused by increasing distance from the ice base that results from melting, following Jenkins et al. (2010). Velocity data are available only for two years, 1996–1997, but they show that the flow at R05 is tidally dominated and that the seasonal variability is small compared with the mean speed. For 1996–1997, the difference between the melt rate calculated using the mean speed and using its 30-day low pass filtered version is negligible (seasonal cycle amplitude differs by less than 1%). The seasonal melt rate variability at R05 is therefore driven almost exclusively by temperature, and the thermistor record alone can be used to estimate the seasonal melt rate signal. Assuming that inter-annual flow speed variability at R05 is small, as suggested by the two-year-long record, an application of Equation 1 to the temperature data can yield a reliable nine-year-long estimate of the melt rate variability. The computed and measured melt rate time series over different years feature the same variability (Figure 3b), supporting the assumptions used in the melt rate calculation.

2.3.2. Site 5

The temperature measurements from the mooring at Site 5c that we exploit here were collected at a distance of 20, 38, 84, and 155 m from the ice-shelf base, and we will refer to these time series as T1, T2, T3, and T4, respectively. Velocity time series are only available from the first and the fourth location (20 and 155 m from ice-shelf base, respectively) and are referred to as U1 and U4. Following Nicholls (2018), we calibrate $C_d\Gamma_{TS}$ for Site 5c using the contemporaneous ocean and ApRES melt rate data from the year 2015. Because the ocean data were collected outside the ice-ocean boundary layer, the $C_d\Gamma_{TS}$ here is the effective Stanton number as it absorbs some of the stratification effects. The parameterization in Equation 1 is applied to T1 and U1. We find that there is little difference between using T1 and T2, which is useful as T1 failed in early 2019 while T2 operated until the end of 2019. The parameterization, calibrated to the mean 2015 data, can be evaluated by comparing the calculated melt rate with the observed melt rate at Site 5a. Site 5a is located less than 5 km from Site 5c, that is, sufficiently close to experience the same variability at monthly time scales. The agreement between the measured and parameterized melt rate for 2019 at Site 5a is as good as for 2015 at Site 5c, the year and location for which the effective Stanton number was tuned (Figure 3a2).

Going further into the past, we apply Equation 1 to mooring data collected at Site 5a between 1999 and 2001, the years when both temperature and velocity measurements are available. Unlike at R05, here at Site 5 both temperature and speed are important contributors to the melt rate variability, and thus measurements from both variables are required. The depth of the instrument cluster nearest the ice base in 1999 corresponds to the depth of T3. There is no U3 time series, therefore we average the U1 and U4 time series to calibrate $C_d\Gamma_{TS}$. The uncertainty in the computed melt rate associated with uncertainty in the vertical velocity profile is at most ± 0.5 ma^{-1}, assuming the velocity profile is monotonic (Figure 3a1). For time scales of days to a week, the match between measured and parameterized melt rates worsens when temperature from deeper instruments is used, because the features responsible for variability at these time scales are surface intensified (Nicholls, 2018). However, for monthly to seasonal timescales, the T3 and U1/U4 combination provides a good basis for melt rate estimation (Figure 3a2). An uncertainty in the calculated melt rate that we are unable to quantify is that of a possible inter-annual or long-term regime change in the way heat is transferred through the boundary layer and that would be manifested as a time varying $C_d\Gamma_{TS}$. However, vertical conductivity, temperature, and depth profiles collected

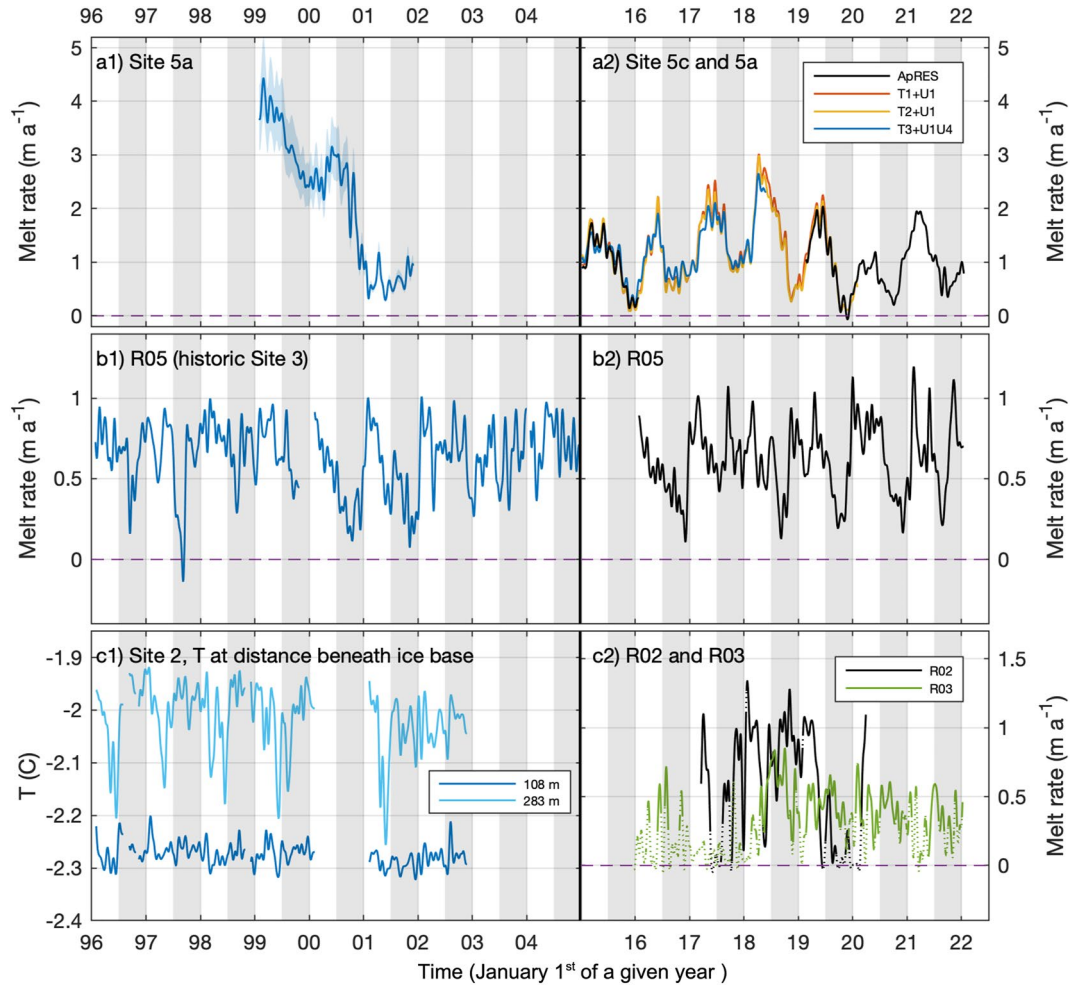

Figure 3. Long-term time series from three areas on the Ronne Ice Shelf. (a) Site 5 melt rate time series. ApRES-derived melt rates are shown in black and calculated melt rates in colors; each color shows results from a parameterization calibrated from instruments at different depths (Section 2.3.2). Blue shading in a1 indicates melt rate uncertainty generated by uncertainty in the vertical profile of horizontal flow speed. (b) R05 melt rate time series; calculated from a parameterization in blue (b1) and measured from ApRES in black (b2). (c) Time series from R02, Site 2, and R03 in the northwestern portion of the Ronne Ice Shelf (Figure 1). (c1) Ocean temperatures for Site 2 from thermistors located 108 and 283 m below the ice base (melt rates are unavailable in this time period and region). (c2) ApRES melt rate time series from R02 and R03, sites that lie glaciologically upstream and downstream, respectively, of Site 2. All time series were filtered using a 30-day low pass cut off.

prior to mooring deployment at Site 5 were similar in structure in 1999 and 2015, suggesting that there has been no regime change (Nicholls et al., 2001; Nicholls, 2018).

3. Melt Rate Time Series

The ApRES melt rate time series are shown in Figure 2. All sites are melting in the long term mean. The mean melt rates are relatively low, typically around or less than 1 ma^{-1}, which is consistent with previous estimates (e.g., Jenkins et al. (2006)) and the fact that the cavity is flushed by relatively cold HSSW. Many of the time series show a significant temporal variability whose character varies widely between the sites.

Starting from R02, located nearest the source of the densest HSSW at the western Ronne Ice Front (Figure 1), we observe multiple timescales of variability with monthly melt rates ranging between 0 and 1.2 ma^{-1} (Figure 2a). There are signatures of seasonal and inter-annual signals with mean melt rate in 2018 being much higher than in 2017 and 2019. R02 has significant variability at weekly to monthly time scales. Occasionally, melt rates

drop below zero, indicating periods of days to weeks in length when marine ice is being accreted to the ice base (Vaňková, Nicholls, & Corr, 2021). Similar, but more frequent freezing periods are present in the signal at R03 (Figure 2b), a site that is located twice as far into the cavity along the eastern flank of the depression (Figure 1). At R03, the freezing events dominate the signal during 2016 and 2017, but between 2018 and 2021 they become restricted to the austral spring and a seasonal melt rate signal emerges. The highest annual mean melt rate for both R02 and R03 occurred in 2018.

R04 is located near Evans Ice Stream on the western side of the Ronne Depression (Figure 1) and the melt rate there is relatively high, averaging 0.9 ma^{-1}, but variations around the mean, even at the spring-neap frequency, are minimal (Figure 2c). Although there is a discernible seasonal cycle at R04, it causes at most 10% change in the rate of melting over the course of the year.

Further into the cavity along the eastern flank of the Ronne depression is located R05 (Figure 1), holding the longest melt rate record because it can be further extended by calculating melt rates from existing R05 sub-ice shelf mooring data (Section 2.3.1). Perhaps the most striking feature of these 15 years of data is the remarkable stability of the melt rate signal (Figure 3b). While averaging 0.6 ma^{-1} the melt rate excursions are confined between 0 and 1 ma^{-1}, the primary variability being driven by a clear seasonal cycle. Any year-to-year melt rate variations at R05 result from suppressions and shifts of the seasonal melt rate minimum.

The data record from the cluster of sites located south of the Korff and Henry ice rises (R06, R07, and R08, Figure 1) is patchy and therefore potentially more difficult to characterize accurately. The most complete data are from R08, with four full years of data over the course of six years. Like at R05, the inter-annual variability at R08 is minimal, and the melt rate variations are primarily seasonal (Figure 2g). At 0.5 ma^{-1}, the R08 mean melt rate is slightly lower than at R05 with seasonal minima and maxima of ∼0.1 and ∼0.9 ma^{-1}, respectively. The 1.5 years of data from R06 suggest seasonal minima and maxima, but the record is too short to assess the extent or character of any inter-annual variability (Figure 2e). For R07 there are some data over each of the four years starting from 2016, and then two full years of data (Figure 2f). Although the data are limited, they show significant inter-annual melt rate variability that contrasts with the neighboring sites R08 and R05. This may be related to the proximity of R07 to the grounding line and steeper slopes of the ice base which result in higher spatial melt rate variability than at the relatively flat portions of the ice shelf further downstream. The inter-annual melt rate variability observed in the Lagrangian frame of reference could therefore represent spatial melt rate variability. Furthermore, the higher melt rate maxima at R07, compared with the neighboring sites, is consistent with R07's deeper ice draft, associated with lower freezing temperatures.

The record from R10, located near Foundation Ice Stream (Figure 1), starts in early 2016 with 2.5 ma^{-1}, the highest measured values from all the ApRES sites, but then the melt rate decreases nearly linearly to 0.8 ma^{-1} by the end of 2017; some variations around this linear melt rate trend are present but difficult to characterize given the short record (Figure 2h). There is a steep basal slope toward the grounding line near which R10 is located, and as in the case of R07, some of the variability in the melt rate time series is likely to be caused by spatial melt rate variations.

R15 has a relatively low melt rate, averaging near 0.2 ma^{-1} and showing very limited variability at monthly time scales (Figure 2j), despite its relative proximity to the ice front and the highly variable R02. The presently available 2-year record does show evidence of a weak seasonal cycle at R15.

The record from R14, located along the northwest coast of Berkner Island (Figure 1), is only three months long (Figure 2i). However, during this short time the melt rate increases from near 0 ma^{-1} to 0.5 ma^{-1}, manifesting significant variability. As the aim of deploying at this location was to monitor melt rates along a potential inflow of less dense HSSW from the Berkner Bank, the relatively large range of melt rates at R14 experienced over a short amount of time suggests that this site is potentially an interesting one to monitor in the future.

Site 5, located further south along the western Berkner Island coast (Figure 1), lies on the predominant flow pathway through the cavity and as such it presents a great range of variability. Melt rates vary seasonally by 1.5 ma^{-1} (Figure 2k). Additionally, over the extended record between 2015 and 2019 melt rates vary inter-annually by 1 ma^{-1}, peaking in 2018 with 2.5 ma^{-1} (Figure 3a2). Extended estimates using oceanographic data from a three-year period starting in 1999 (Section 2.3.2) suggest that melt rates at this site were as high as 4 ma^{-1} in 1999 (Figure 3a1).

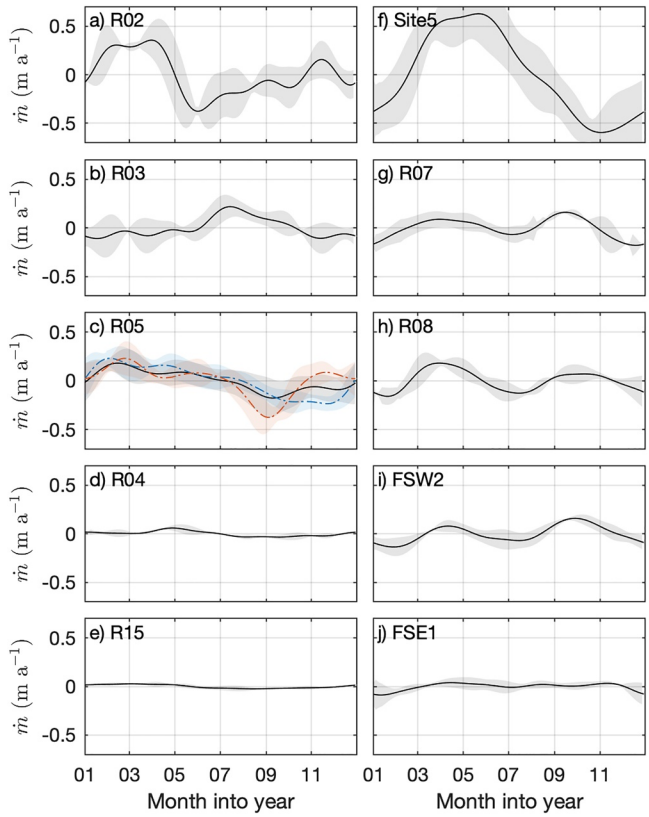

Figure 4. Composite seasonal melt rate anomaly using 60-day low-pass filtered time series from sites that had at least 2 years of melt rate data. For R05 we also show a composite from group A and group B years only in red and blue dash-dotted lines, respectively. Shading shows one standard deviation.

On Filchner Ice Shelf (Figure 1), the melt rate from FSW2 (Figure 2l), located in the south west, is most similar to the R08 time series (Figure 2g). There is a strong seasonal signal, but the melt rate does not vary inter-annually (Figure 2l). There is a single freezing event that took place at the beginning of 2021. FSE1, south east of FSW2, has six years of data and the melt rate is near 0 ma^{-1} (Figure 2m). We could not identify the sign of the melt rate with sufficient confidence during most of the time between 2016 and 2019, but between 2020 and 2021 the site was melting with minimal temporal variations. Only one year of data is available from FNE3 and it indicates a relatively high melt rate and substantial variability (Figure 2n), consistent with its proximity to the Filchner Ice Front.

4. Seasonal Variability

To characterize seasonal melt rate variability over FRIS, we construct seasonal composites for ApRES sites that have at least two years of data (Figure 4). We find two types of seasonal signals; one that has a single seasonal maximum and minimum, and one that has two equally high seasonal maxima and minima. Sites with a single seasonal maximum include locations above the Ronne Depression, R15, and Site 5. Two seasonal maxima are clearly present at R07 and R08, both located behind the Korff and Henry Ice Rises, and at FSW2 southeast of Berkner Island (Figure 1).

4.1. Single-Maximum Seasonal Signal

The main known source of seasonal variability beneath FRIS is the seasonal formation of HSSW (Nicholls, 1997). The onset of sea-ice formation and convection above the continental shelf typically begins in early March (Makinson et al., 2006). HSSW then enters the cavity and propagates along the eastern flank of the Ronne Depression, which has been observed (Nicholls, 1997) and modeled (Jenkins et al., 2004). What remains unclear is how well the deeper flow variability is coupled to the local melt rate. Previously acquired temperature data from R05 show that the arrival of HSSW at depth is associated with relatively abrupt upward motion of isothermals throughout the entire water column thickness, which results in higher temperatures in the boundary layer and an increase in melt rates at this particular site (Figure 5). Based on these data, we interpret, where possible, the asymmetric, single seasonal maximum melt

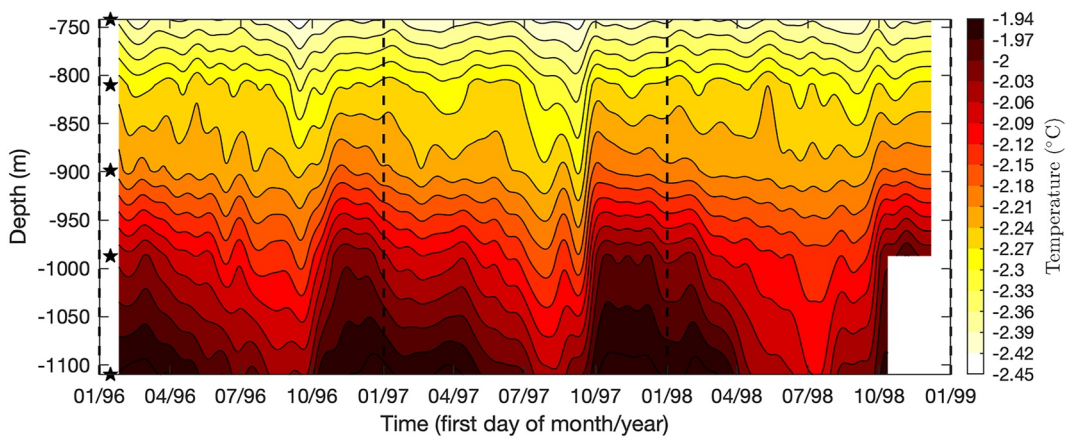

Figure 5. Evolution of the vertical temperature profile beneath the R05 drill site; the time series were smoothed using a 30-day low-pass filter. Mooring depths are indicated as black stars.

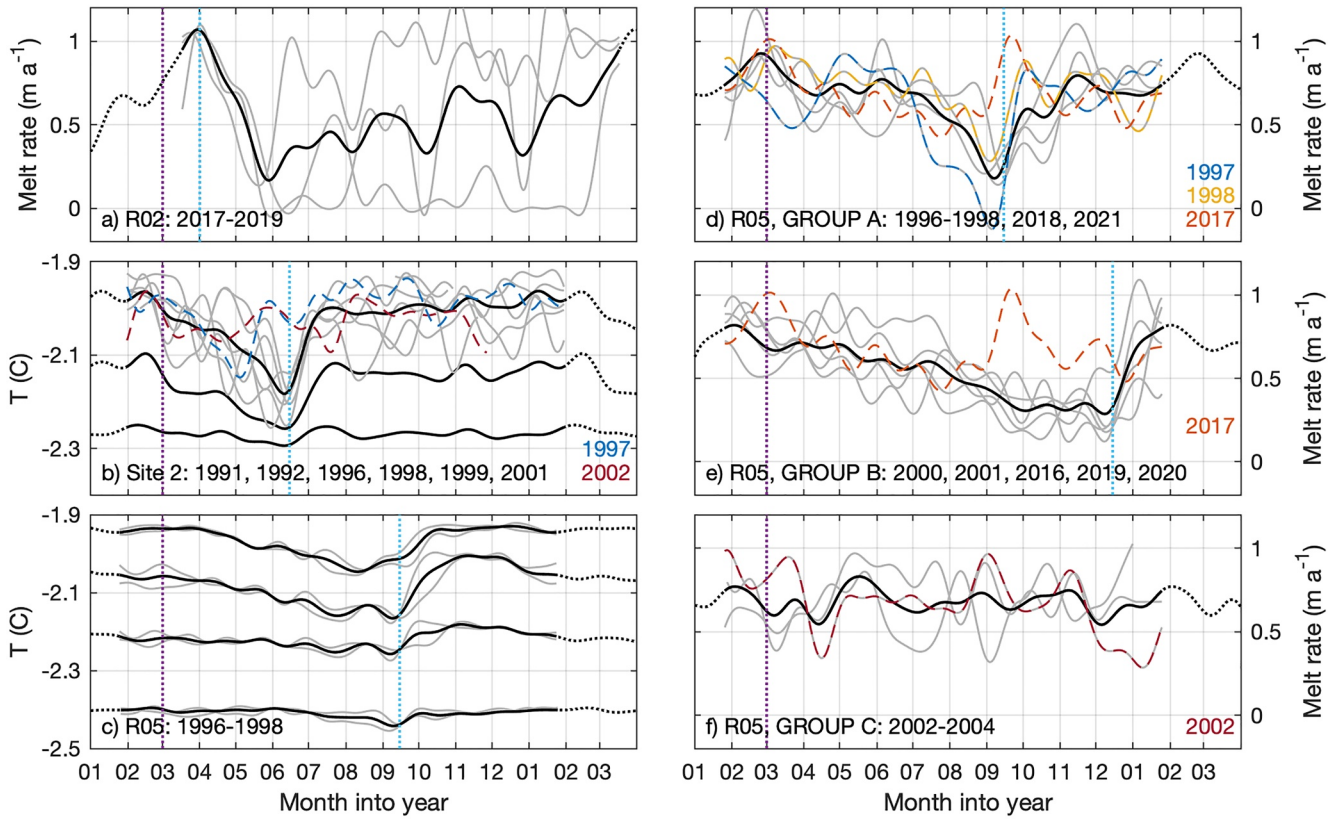

Figure 6. Seasonal cycle along the High-Salinity Shelf Water flow pathway inside the Ronne Depression. In all panels, the solid black line shows a seasonal composite formed by averaging all the 1-year long signals that are shown in gray (black dotted line repeats the seasonal signal). The range of years printed in black specifies the years which were used for the averaging. Outliers or otherwise significant years are highlighted in colors. The dotted purple line indicates the onset of convection from Makinson et al. (2006) and the dotted blue line the approximate timing of HSSW arrival at each site. (a) R02 melt rate. (b) Site 2 ocean temperature at 108, 213, and 283 m from the ice base, temperature increasing with depth. For clarity data from individual years are shown only for the deepest instrument. (c) R05 ocean temperature. (d)–(f) R05 melt rates divided into three groups based on the shape of the seasonal cycle. 2017 is not included in any group but has features of groups A and B so it is shown on both panels (e) and (f) in orange dashed line.

rate signal from sites above the eastern flank of the Ronne Depression in terms of the propagation of a seasonal Ronne-sourced HSSW pulse at depth, in line with Nicholls and Makinson (1998).

The winter convection in the Ronne shore lead begins in early March, as observed near the ice front between 1995 and 1997 at FR5 (Figure 1) by Makinson et al. (2006). A month later, there is a sharp seasonal decrease in basal melting at R02 (Figure 6a), the most northwestern ApRES site, that occurred regularly during all three observed years (Section 4.3 investigates reasons for the negative sign of the abrupt melt rate change at R02). As the HSSW pulse propagates further it arrives at Site 2 in the middle of June (Figure 6b), where its signature is most pronounced at depth and weakens toward the ice base, where the HSSW is overlain by ISW (Nicholls, 1996). This timing of HSSW arrival at Site 2 is relatively robust, having occurred in mid June for four out of the six observed years. Further downstream at R03, the seasonal signal is small compared with the shorter time scales of variability of days to weeks, indicating that other processes dominate at this site. The first two years of data are almost entirely dominated by intermittent freezing (Figure 2b). However, the following four years do show some seasonal variability; intermittent freezing is restricted primarily to austral summer months with the site having positive melt rates during the rest of the year (Figure 2b). The shape of the seasonal signal, obtained by averaging years 2018–2021, shows a local melt rate maximum in mid July (Figure 4b). Although R03 is nearly twice as far from R02 as Site 2, seasonal melt rate increase begins at R03 in mid June (Figure 4b), at around the same time of year as the temperature pulse appears at the Site 2 data collected two decades earlier (Figure 6b). Given that timing, it is unclear whether the seasonal signal at R03 in the last four years of data is directly related to the arrival of HSSW. It is also unclear why the seasonal signal was absent in the first two years. Frequent intermitted freezing at R03 (Figure 2b) suggest that, like at Site 2, the upper part of the water column beneath R03 is occupied by

ISW, at least some of the time. The melt rate variability at R03 is then probably controlled by the variability of the ISW outcrop position with respect to the site, which is controlled not only by stratification and HSSW layer thickness but also by flow speeds and baroclinic instabilities such as those inferred from the Site 2 observations (Nicholls, 1996).

The interpretation of the data becomes less straightforward for R05. While the R05 ocean temperature and calculated melt rate data during 1996–1998 show a consistent arrival of the HSSW pulse in mid September (Figures 6c and 6d), there is a year-to-year variability in the shape of the seasonal cycle that becomes apparent only when a long-term melt rate time series is examined (Figure 3b). Figure 6 shows that we can distinguish three groups of years. Group A includes years 1996–1998, 2018, and 2021, which have an asymmetric seasonal cycle with an abrupt melt rate increase occurring in mid September and a more gradual melt rate decrease from about April on (Figure 6d). For group B, formed by years 2000, 2001, 2016, 2019, and 2020, the seasonal cycle and its asymmetry are even more pronounced than for group A. The melt rate peaks in late January from where it gradually decays, reaching a minimum between October and December (Figure 6e). However, its increase in mid December is as abrupt as for group A, except that it occurs full 3 months later. The record for the year 1999 is incomplete but the available data suggest that it also belongs to group B. Finally, group C formed by years 2002, 2003, and 2004 does not have a clear seasonal cycle, the melt rate remains high at around ∼0.7 ma^{-1} with variability occurring primarily at faster than seasonal time scales (Figure 6f). The year 2017 does not belong exclusively to a single group as it has features of both group A and group B. A local melt rate high occurs past September like for group A (Figure 6e), but then melt rates drop again and temporarily increase past December like for group B (Figure 6f). Potential causes of the year-to-year differences at R05 are further discussed in Section 5.1.

The seasonal signal at R04 and R15 is very weak and does not have the same sharpness and asymmetry, characteristic of HSSW propagation as in the data from sites along the eastern flank of the Ronne Depression. Melt rate decrease at R15 occurs about a month later than at R02. The seasonal melt rate increase at R04 lags three months behind R05 during the respective year and could thus be interpreted as a clockwise propagation of the HSSW pulse around the back of the Ronne Depression, following contours of constant water column thickness.

The largest amplitude seasonal melt rate signal from the entire ice shelf is observed at Site 5. The signal there is symmetric and the variability in its shape and amplitude is small, particularly compared with that of R05. The single-maximum seasonal signal in ocean properties at Site 5 is present throughout the water column and seasonal variations in both temperature and flow speed are important contributors to the seasonal melt rate variability. The amplitude of the seasonal temperature signal increases toward the ice base. The waters near the ice base are thought to be sourced from a less saline flavor of HSSW originating at Berkner Bank (Nicholls et al., 2001). Thus the greater proximity of the lighter water to its source can explain the larger amplitude of its seasonal cycle compared with the water at depth that originates in the Ronne Depression (Figure 1). Nevertheless, waters from both sources have been heavily modified through interactions with the ice-shelf base and are over 0.2°C cooler than the HSSW (Nicholls et al., 2001).

4.2. Two-Maxima Seasonal Signal

A two-maxima seasonal melt rate signal is characteristic for sites located at the back of the FRIS cavity, toward the southeast. There are mooring data available from drill site FSW1, located only ∼7 km east of the FSW2 ApRES site, and these can add insight to the melt rate observations. Figure 7 shows plots of ocean properties at two instrument clusters from the FSW1 mooring, located 70 and 410 m below the ice base. The main feature of the temperature and salinity data at the different depths is that the time series from instruments near the ice base have a two-maxima seasonal cycle (Figure 7a1 and 7a2), consistent with the measured melt rate at FSW2, while the time series from instruments near the ocean floor have a single-maximum seasonal cycle (Figure 7b1 and 7b2). The flow speed time series from different depths are very similar and do not have a clear seasonal cycle(Figure 7a4 and 7b4), suggesting that the seasonal basal melt rate variability is driven primarily by temperature variations. We calculate basal melt rates using methods in Section 2.3 and find that the parameterization does not capture well the amplitude of the seasonal melt rate variability (Figure 7a5). This most likely can be ascribed to the relatively large distance (70 m) of the upper most instrument from the ice base. The implication is that the amplitude of the temperature, and possibly also flow speed, seasonal signal increases with proximity to the ice base.

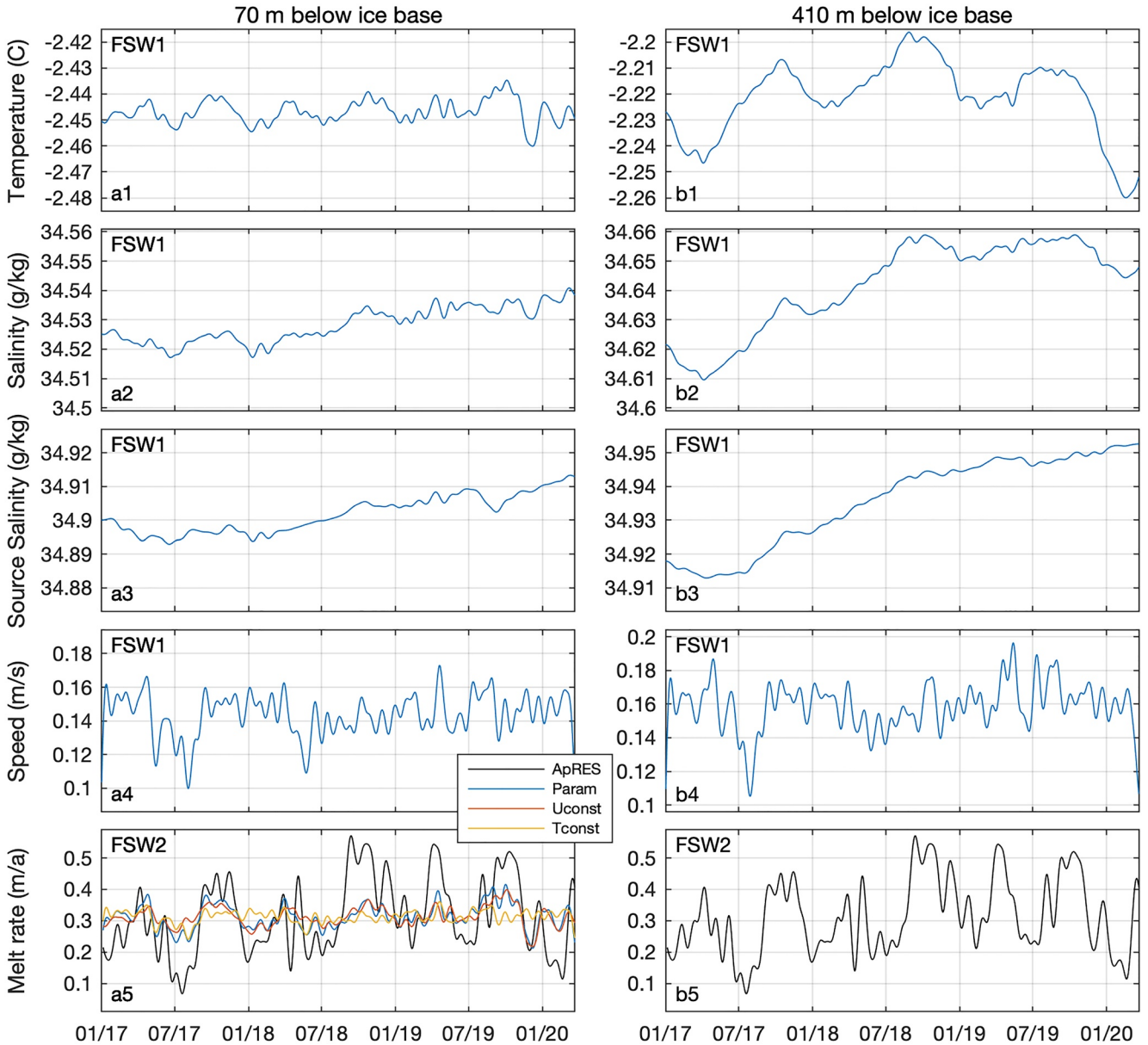

Figure 7. Time series of ocean properties from the FSW1 mooring instruments at two different depths and melt rates from an ApRES at FSW2. ApRES melt rate is in black and calculated melt rate from ocean data at 70 m depth in blue. In red is melt rate calculated using constant flow speed and in yellow melt rate calculated using constant temperature.

Potential causes of this two-maxima seasonal signal include different source waters driving melting during different parts of the year, waters arriving at the site via multiple pathways, or both. To investigate the possibility of different sources, we calculate salinities of the source HSSW implied by the meltwater mixing-line relationship (Gade, 1979). The source water salinity is largely free from the seasonal signal at both the upper (Figure 7a3) and lower (Figure 7b3) instruments, the primary variability of the source water salinity signal being inter-annual, the causes of which are discussed in detail by Hattermann et al. (2021). Therefore, it appears that given a single-maximum seasonal forcing at the ice front, it is likely that the two-maxima seasonal signal at the FSW sites results from waters arriving to this location via multiple pathways, potentially but not necessarily related to the primary flow pathways through the cavity (Janout et al., 2021).

We lack oceanographic context for R07 and R08, and the sites are located at a very different part of the cavity than the FSW sites, therefore the interpretation of the two-maxima seasonal cycle there remains speculative. A

mechanism for secondary HSSW inflow has been identified by Jenkins et al. (2004) and it takes place at the end of the convective season. While this secondary inflow is sometimes observed at R05, it is much weaker than the primarily winter inflow throughout the three observed years (Figure 5). Even at R05 this secondary inflow doesn't induce a persistent seasonal signal with two maxima that would be visible in the seasonal composite melt rate. Therefore, it appears unlikely that this secondary inflow would be so pronounced at sites located even further away from the source of the variability. If the two-maxima signal at these sites were caused by multiple pathways, it would require a more refined picture of the FRIS circulation and the currently known two main pathways (Janout et al., 2021) would not be sufficient to explain the data.

4.3. Northwest Ronne Ice Front Dynamics, R02

We now address the differences in the way the HSSW pulse arrival is expressed at R02, compared with the remaining sites along the eastern flank of the Ronne Depression. At Site 2 and R05 the arrival of the seasonal HSSW pulse is manifested as an abrupt increase in temperatures (as a melt rate proxy) or melt rates (Figures 6b–6d) and then a more gradual decay in those quantities. Contrary to these sites, at R02 the shape of the seasonal cycle is inverted in that there is first an abrupt decrease in melting as a result of HSSW pulse propagation and later a more gradual melt rate increase (Figure 6a). The abrupt decrease in melt rates takes place in early April during all three observed years (Figure 6a). Melt rates reach a minimum between mid May and mid June, sometimes experiencing days to weeks long episodes of marine ice accretion. In 2017 and 2018, the melt rate gradually increases back to its maximum by October, while experiencing substantial variability at shorter time scales. In 2019, melt rates stayed low throughout most of the year with multiple episodic accreted-ice events including one that lasted over two months between December and February (Figure 2). High, $\sim$1 ma^{-1} melt rates returned relatively abruptly at the beginning of March 2020.

The characteristics of the R02 seasonal signal are a signature of more complex flow dynamics near the western Ronne Ice Front. These result from the presence of a tidal front, inferred by Nicholls et al. (2004) from a series of vertical ocean profiles acquired midway between R02 and the ice front (for borehole locations see green stars in Figure 1). A thin water column region along the central-eastern Ronne frontal region (Figure 1) is characterized by high tidal currents (Padman et al., 2002), which enhance vertical mixing and modify local stratification. The result of this spatially heterogeneous tidal mixing is a west-east gradient in stratification with a well mixed region south of the central-eastern ice front and a more stratified region above the Ronne Depression, separated by a tidal front. The associated density structure sets up a circulation which affects the flow pathways of HSSW beneath the ice shelf (Nicholls et al. (2004)). For example, observations from a location directly north of R02 show an outflow from the cavity, although the site is located on the eastern flank of the Ronne Depression, and thus in absence of a tidal front we would expect a dense water inflow instead (Nicholls et al., 2004). The seasonal melt rate observations from R02 indicate that this site also does not lie directly above the HSSW inflow. If that were the case we would expect to see a seasonal melt rate increase in early autumn. Instead, as the pulse of HSSW enters the FRIS cavity, the melting at R02 sharply reduces. A potential clue to resolving this apparent contradiction is provided by the presence of episodic accreted-ice events that follow the seasonal melt rate decrease at R02. Basal accretion at R02 is caused by the precipitation of frazil ice onto the ice base (Vaňková et al., 2021), a process that requires supercooling of ISW somewhere near R02.

An ISW outflow, located just east of R02, has been observed during summertime ship-based campaigns (Foldvik et al., 1985; Janout et al., 2021). Furthermore, an ice-front mooring FR5 (Figure 1) was deployed in 1995 to monitor the ISW outflow evolution. The data show a seasonal appearance and disappearance of ISW from the site, suggesting that the ISW outflow may be a seasonal feature (Nicholls et al., 2003). FR5 was occupied by HSSW between May and October (Figure 8 in Nicholls et al. (2003)). After that the site cooled below -1.9°C, indicating the presence of ISW, with lowest temperatures attained during austral summer. Around April the ISW disappeared relatively abruptly from FR5. Because the mooring is stationary, this implies that either the ISW outflow is a transient feature, or that the position of the outflow varies in space. The new R02 melt rate data support the hypothesis that the ISW outflow current undergoes a seasonal lateral shift. We observe that the abrupt melt rate decrease at R02 followed by basal accretion events typically occurs around the time that ISW abruptly disappears from FR5. Together, observations from these two sites, although separated in time by over two decades, consistently indicate that there is an eastward shift of the ISW outflow current during autumn (Figure 6a) that results from the inflow of the HSSW pulse west of these sites. The ISW outflow then gradually returns to its

summertime position as indicated by relatively slow melt rate increase at R02 and reappearance of ISW at FR5. Therefore, the seasonal melt rate signal at R02, albeit more complex, is still consistent with the seasonal HSSW inflow dynamics.

5. Inter-Annual Variability

5.1. R05

We begin the discussion of inter-annual melt rate variability at FRIS with the longest available time series, the 15-year long melt rate record from R05. Here, the melt rate ranges between ∼0 and ∼1 ma^{-1} and it varies seasonally within these bounds (Figure 3). Inter-annual variability is manifested as year-to-year differences in the timing of the seasonal melt rate low preceding a melt rate increase associated with the HSSW pulse arrival, or its absence (Figures 6d–6f). For group A, the seasonal melt rate increase occurs in mid September, for group B in mid December, and group C does not have a clear seasonal cycle with melt rates staying high throughout the year.

To gain further insights into the evolution of the water column beneath R05, we turn again to the mooring data from 1996 to 1998 (Figure 5), although it only captures the group A years. In Section 4 we noted that the arrival of the HSSW water pulse occurs at approximately the same time throughout the water column all the way to the ice base. However, in general the amplitude of the temperature change at depth is not necessarily mirrored by the amplitude of melt rate change in the same way. For example, the 1997 winter was relatively warm at depth compared with the much colder 1998 winter (Figure 5). At the same time the seasonal melt rate minimum was much higher in 1998 than in 1997 (Figure 3b1). This shows that the different rates of melting in the austral winter at R05 cannot be interpreted solely as changes in the thickness of the HSSW layer, because the changes in ocean stratification beneath R05 are also significant (stratification changes are proportional to temperature gradients here because the only source water, HSSW, is transformed solely by melting interactions with the ice shelf).

In the austral winter of 1998 the lightest and densest waters that were present in the previous two summers are absent and the stratification is weaker throughout the water column. This can be attributed either to enhanced vertical mixing, or to a spatial rearrangement of isopycnals. The observations show that the vertical temperature gradient had been eroded throughout the water column, and thus a potential candidate for the observed inter-annual stratification changes is variable shear-driven mixing. Although the background flow at R05 is weak and its variations are small at monthly timescales (Nicholls et al., 1997), the observed stratification changes, if driven by enhanced shear mixing, could have originated elsewhere, further upstream along the HSSW inflow pathways.

The years 2002–2004 in group C do not have a seasonal melt rate cycle (Figure 6f). As the deeper moored instruments no longer operated at R05 by then, we do not have direct information about the occurrence or timing of the seasonal HSSW arrival. However, there is a one year overlap between group C years and a thermistor record at Site 2 that ran to the end of 2002. Figure 3c1 shows that 2002 is anomalous in the Site 2 data in that it too shows no seasonal drop associated with the thinning of the HSSW layer. This suggests that, at least in 2002, but possibly also in the two following years, the absence of a seasonal melt rate cycle at Site 2 may have resulted from limited or no seasonal thinning of the HSSW layer at depth throughout the southern Ronne Depression. Alternatively, we can hypothesize, based on the observed vertical temperature evolution from 1996 to 1998, that these years correspond to even weaker winter stratification than in 1998, obscuring the seasonal cycle, which may otherwise be present at depth. Under this interpretation, the R05 melt rates could be an indirect indicator of the strength of the ocean stratification beneath.

Finally, we turn to group B, which is characterized by a pronounced seasonal melt rate signal whose abrupt seasonal melt rate increase is delayed by approximately three months compared with group A (Figure 6e). The group B years were also not captured on the deep R05 moorings, but one of the years, 2001, was covered by the thermistor record at Site 2 (Figure 3c1). From these data we conclude that there is no anomaly in the HSSW arrival in 2001 at the Site 2 location. This implies that the observed delay at R05 was not caused by a change in the timing of the HSSW inflow beneath the Ronne Ice Front. It is unlikely that the R05 signal is caused by different HSSW flavors arriving in different years. That is because the Berkner-HSSW generated seasonal signal, as observed at Site 5, does not have the same asymmetry as the Ronne-HSSW generated signal. Furthermore, a westward Berkner-HSSW flow would need to defy the west-east density gradient. As a result, it is almost certainly Ronne HSSW that arrives at R05 in both A and B years. A delay in a seasonal cycle at R05 can then

be caused either because the water flows much slower between Site 2 and R05 in some years than in others, because it takes a different path while traveling at the same speed, or because of both. One possibility for alternative pathways is as follows. In some years the HSSW pulse reaches R05 by following the eastern flank of the Ronne Depression (red dotted and then red dashed line in Figure 1), while in other years it crosses through a bathymetric low located between R02 and R03 as suggested by Nicholls and Østerhus (2004) (solid red line in Figure 1). Afterward, the main branch of the HSSW pulse flows southeastward toward Site 5 and a smaller branch flows toward R05 passing near historic Site 1 (purple dotted line and then red dashed line in Figure 1), where a southward flow into the cavity had been observed in the past (Nicholls et al., 1997). However, to show the true causes of this delay, we would require a denser observational network or a numerical model able to reproduce such a feature, which is beyond the scope of this paper.

5.2. Site 5

The inter-annual variability in melt rate at Site 5 is superimposed on a relatively regular seasonal cycle (Figure 3a). Between 2015 and 2021 melt rates averaged 1.1 ma^{-1} and they varied inter-annually by $\sim$1 ma^{-1}, peaking in 2018 and reaching a minimum in 2020. Calculated melt rates from previously acquired data capture the aftermath of the anomalously convective year 1997 and indicate annual mean melt rates as high as 3.5 ma^{-1}. This is the highest in-situ annual mean melt rate estimated from any observed FRIS location.

As the waters in the upper and lower parts of the water column are sourced from different locations, Berkner Bank and the Ronne Depression (Figure 1), respectively, the use of melt rate data to understand variability at depth beneath Site 5 is potentially limited. While the temperature variability at daily to seasonal time scales is surface intensified, the inter-annual temperature variability is minimal at the uppermost instrument and it increases with depth. In contrast, the depth dependency of flow speed variability at seasonal and inter-annual time scales is minimal, and both the upper and lower sensors U1 and U2 show substantial inter-annual variability. Calculations using Equation 1 confirm that it is the flow speed contribution to melting that generates the inter-annual signal in the melt rate time series. We conclude from these observations that at Site 5 the inter-annual melt rate signal is informative about the inter-annual variability in flow speed of the deep waters, while the seasonal signal informs about the seasonal temperature and flow variability in the upper layers sourced from Berkner Bank (Figure 1).

The Site 5 melt rate time series have two main inter-annual maxima, one in 1999 and the other in 2018. Both of these can be related to anomalously low sea-ice concentration over the Weddell Sea continental shelf in the austral summer of the preceding year (1997/1998 and 2016/2017, respectively) and subsequent anomalously high HSSW production in the autumn. The extensive Ronne polynya during summer 1997/1998 was described by Ackley et al. (2001) and the near-record low summer Weddell Sea sea-ice extent in 2016/2017 is documented in Turner et al. (2020). To systematically analyze sea-ice concentration near the Ronne Ice Front, Hattermann et al. (2021) computed a sea-ice formation index, which serves as a proxy for HSSW formation rate. According to this index, the highest HSSW production indeed occurred in 1998 and in 2017. The link between the 1998 sea-ice low and increased flow speeds at Site 5 was explained by Nicholls and Østerhus (2004) in terms of the propagation of a HSSW pulse from the Ronne Ice Front across the ice shelf, following contours between R02 and R03 directly to Site 5. Similar conditions, enhanced HSSW formation and subsequent flow speed increase at Site 5, are associated with the 2018 melt rate maximum at Site 5.

To investigate how these anomalously high HSSW formation events affect the rest of the Ronne cavity, we turn to the remaining ApRES melt rate time series that sampled around years 2017 or 2018 (Figure 2). We observe that both R02 and R03 show increased melting during 2018, while sites further back in the cavity (R04, R05, R07, and R08) do not show any such increase. This agrees with the conclusions of Nicholls and Østerhus (2004) that during enhanced HSSW inflow beneath the ice shelf the flow speed increase occurs on the flow pathway from the western Ronne Ice Front toward Site 5 through the middle of the ice shelf (solid red line in Figure 1), and not behind the Korff and Henry Ice Rises (dashed red line in Figure 1). The observations show that melting also increased at R03 in 2018, suggesting that the flow pathway along which inter-annual variations propagate extends past the bathymetric high between R03 and Site 1, encircling it and turning northeast from there to follow contours of constant water-column thickness (dotted red line in Figure 1). This would be consistent with recent models of the FRIS cavity circulation which also show this circulation pathway (Bull et al., 2021; Hausmann et al., 2020). The year's delay between the sea-ice low and the high melt rates may be related to the time it takes to gather dense water in the Ronne Depression (Janout et al., 2021), but the exact processes by which the HSSW

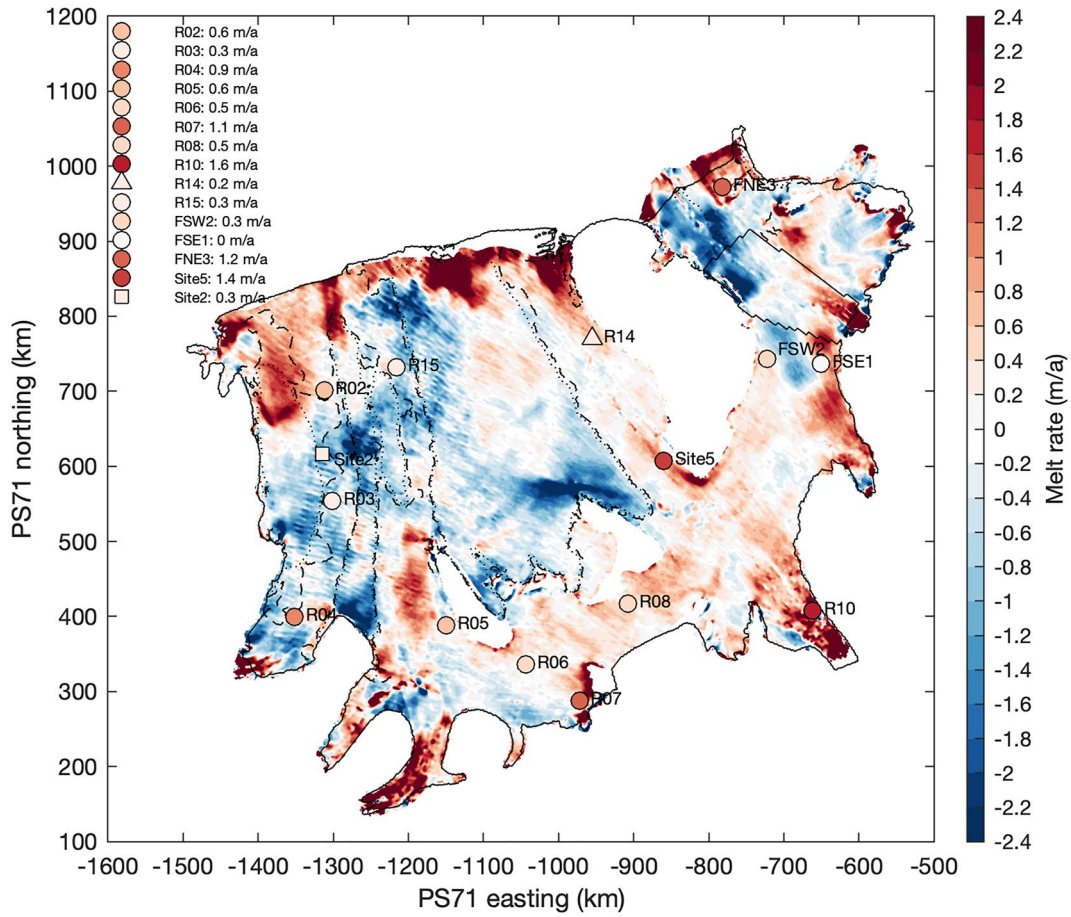

Figure 8. Mean basal melt rate derived from in-situ measurements (symbols) compared with estimates from satellite data by Adusumilli et al. (2020). The dashed contour encloses regions where any marine ice is present according to the compilation of Lambrecht et al. (2007), the dotted contour encloses marine ice thicker than 10 m, and the solid contour encloses the region where data for assessing the presence of marine ice were available. Circles mark sites where the melt rate time series represent mean over at least 1-year long record. R14 is marked with a triangle to indicate an ApRES record shorter than a year. Melt rate from Site 2, marked with a square, was estimated from a vertical temperature profile in the ice column by Vaňková, Nicholls, and Corr (2021).

is transported beneath the ice shelf and how those respond to anomalies in the HSSW volume on the continental shelf remain unknown.

6. Comparison With Satellite Estimates

Because basal melt rates are typically inferred from indirect measurements, it is important to compare estimates from complementary techniques. Here we compare our in-situ melt rate estimates with the most recent estimates from satellite data, which provide not only mean melt rates but also variability at quarter-yearly resolution (Adusumilli et al., 2020).

Figure 8 compares mean melt rate estimates from the two techniques. Additionally, we also include an in-situ estimate from Site 2, which did not have an ApRES, but where the mean melt rate was calculated from the measured vertical temperature profile of the ice column in the 1990s and yielded 0.3 ma^{-1} (Vaňková, Nicholls, & Corr, 2021). The remote and in-situ estimates do not cover the same time period, which is a limitation of the comparison. However, this limitation may not be as severe considering the relatively small amplitude of inter-annual variability that we have measured in-situ, perhaps with the exception of Site 5. There is a good agreement east of R06, including the very low melt rates at FSE1 and FSW2, high melt rates at R07, R10, Site 5, and FNE3, and moderate melt rates at R06 and R08. On the western half of the Ronne Ice Shelf the agreement

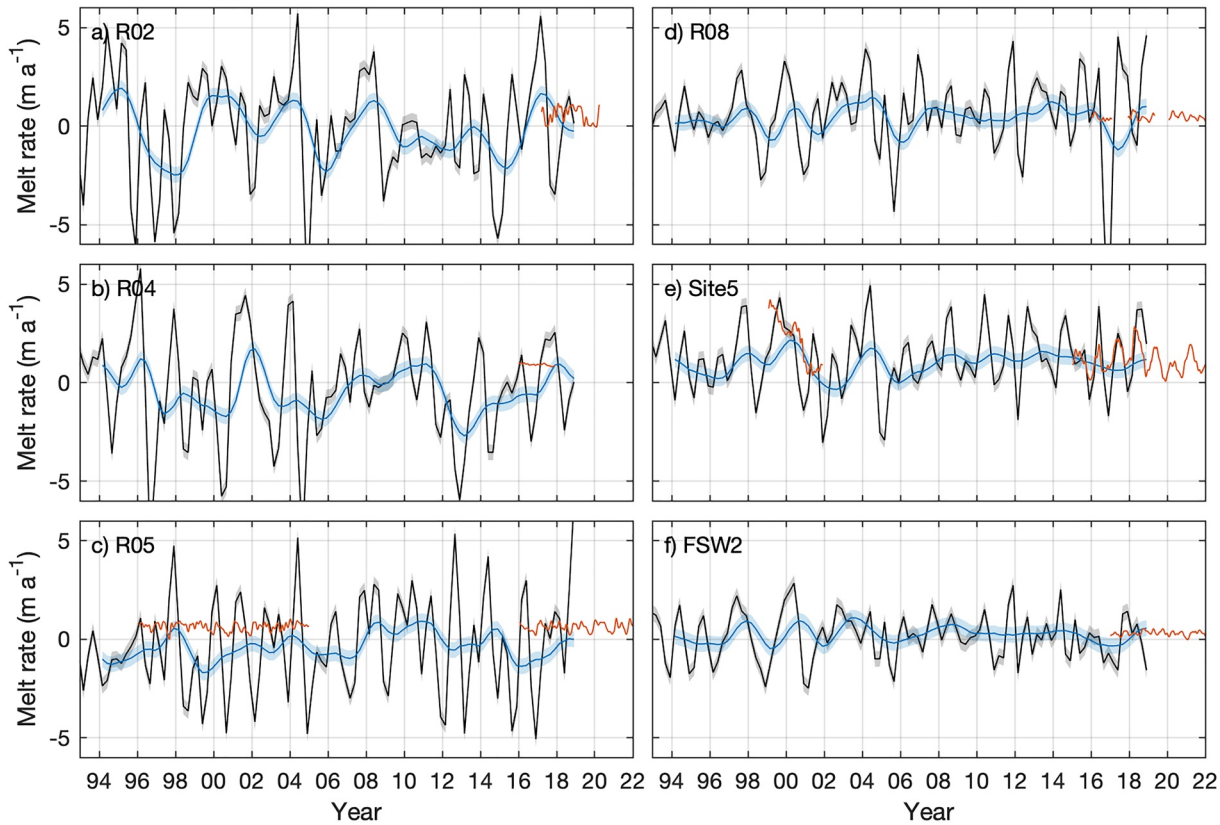

Figure 9. Basal melt rate time series derived from in-situ measurements (red) compared with estimates from satellite data; the quarter-yearly satellite estimates (black) and their low-pass filtered (blue) version as in Adusumilli et al. (2020), who also reported a FRIS-wide uncertainty estimate of 0.4 ma^{-1} (shading).

is less good. Several sites that are melting according to the in-situ measurements, the satellite estimates indicate are freezing. This includes R03, R04, R05, and Site 2. Furthermore, R02, although melting according to both estimates, shows higher melt rates in the ApRES than in the satellite data.

Altogether it appears that the estimates of Adusumilli et al. (2020) overstate the area of basal freezing at the western part of the Ronne Ice Shelf. This claim is further supported by the marine ice thickness compilation of Lambrecht et al. (2007). The regions where marine ice is present at the ice-shelf base are marked in Figure 8. There are three major stripes of marine ice area extending from south to north, but they are well separated by continuous south-to-north stripes without permanent marine ice, which must therefore be melting on average. These south-to-north melting areas are consistently reproduced across different ocean models of the FRIS cavity (Bull et al., 2021; Daae et al., 2020; Hausmann et al., 2020). The in-situ observations were collected in these regions free of marine ice, which supports them having the correct sign of long-term melting. For consistency, areas that are freezing on average should have marine ice deposits glaciologically downstream, as is the case north of Henry Ice Rise, for example (Figure 8). However, this is not the case for many of the regions in the western Ronne Ice Shelf identified as freezing in Adusumilli et al. (2020).

Comparison of representative melt rate time series derived using the in-situ and the satellite data are shown in Figure 9. For the satellite estimates we plot both the quarter-yearly resolution and their 1-year running mean as presented in Adusumilli et al. (2020). The amplitude of temporal variability in the satellite melt rate estimates, both the quarterly and the low-pass filtered versions, is much larger than observed in-situ for all ApRES sites, except for Site 5. For example, at R05, which has the longest available in-situ record, the in-situ melt rates are bounded between 0 and 1 ma^{-1}, while the satellite estimates show seasonal signal ranging between −5 and 5 ma^{-1} and low-pass filtered melt rates varying between −2 and 1 ma^{-1} (Figure 9c). The limited temporal coverage of the ApRES data at most locations does not allow for a contemporaneous comparison of the inter-annual melt rate variability. However, the satellite estimates show similarly high amplitude of inter-annual melt rate variations as

at R05 at all the remaining sites, while the shorter in-situ records indicate stable rates of melting with limited inter-annual variability.

One location where the estimates agree relatively well is Site 5 (Figure 9e). There the satellite estimate captures well the high melting following the 1998 anomaly, which appears as a wider peak of elevated melt rates over the years 1999–2000, even though the local maximum is delayed compared with the in-situ data. The second portion of the in-situ Site 5 data from 2015 to 2019 also agrees well with the satellite estimate, even capturing the phase of the seasonal cycle correctly, although during some years the seasonal melt rate amplitude is too large by a factor of up to two, and also indicates frequent periods of strong freezing. It is interesting that the amplitude of melt rate variability in the satellite estimates is actually larger for the western Ronne sites, where in-situ observed variability is lower, than for Site 5, where the in-situ data show the highest inter-annual variability. This implies that the source of the error in the satellite data is not spatially uniform across FRIS.

The ApRES is advected slowly by the ice-shelf flow (a few hundred meters per year). As a result the instruments move in total by a distance smaller than a grid cell on the 10-km grid on which the satellite-derived time series are reported. Furthermore, there is little spatial variability in the satellite time series, so spatial averaging does not significantly decrease the excessive temporal variability. The in-situ ApRES melt rate estimates are representative over the footprint of the radar, which is comparable in size to the ice thickness (~400 m to 1 km, depending on the site). This was determined by inspecting melt rate variability from off-nadir reflectors further along the ice base (Vaňková, Cook, et al., 2021). While in rare cases a site may be shielded from large scale variability, it is extremely unlikely that this would happen at multiple locations. Otherwise, larger spatial averaging will always result in lower, not higher temporal variability. Therefore, the excessive temporal variability in the satellite-derived melt rate estimates over FRIS is most likely incorrect.

Using satellite observations to estimate short-term changes in basal melt rates involves accounting for those processes causing short-term changes in ice shelf surface elevation that are unrelated to basal mass balance. The effect of any errors in accounting for such processes (e.g., surface mass balance and firn densification) will be magnified by nearly an order of magnitude when converted to changes in ice thickness. Long term averages of, for example, snow accumulation are relatively robust, but accurately modeling temporal variations in precipitation is notoriously difficult, and likely to be the dominant source of the lack of agreement between the basal melt rate variability presented here, and that derived from methods using satellite altimetry.

7. Summary and Conclusions

We deployed multiple ApRES to assess the nature of seasonal and inter-annual melt rate variability at FRIS. ApRES time series up to six years in length have been presented here (Figure 2), but some of the locations continue to be sampled and should yield further insights into inter-annual variability in the future. Melt rate time series were extended to the past at two sites, where oceanographic measurements near the ice base were available and it was possible to calibrate a melt rate parameterization (Figure 3). Data, previously acquired from sub-ice shelf moorings, were used to aid interpretation of the melt rate time series.

A seasonal melt rate signal is present at nearly all FRIS sites (Figure 4). Locations along the Ronne Depression feature a single seasonal melt rate maximum and minimum and these are associated with the propagation of seasonal HSSW inflow at depth. At all these sites, except at R02, melt rates rise abruptly when HSSW thickness increases at depth. At R02, located near the ice front, the inflow dynamics is affected by the presence of a nearby tidal front and an ISW outflow. There, the effect of the HSSW inflow is to displace outflowing ISW eastward, causing an abrupt drop in R02 melt rates. At the back of the FRIS cavity, there were three sites that feature a seasonal signal with two comparably high seasonal maxima and minima. At one of the sites, FSW2, oceanographic data from a sub-ice shelf mooring indicate that this two maxima seasonal signal is likely caused by two different pathways of the same source water (Figure 7). Causes of this signal at the two remaining sites R07 and R08 remain unclear.

The largest range of inter-annual melt rate variability is present at Site 5, which lies on the main flow pathway beneath the ice shelf (Figure 1). Although the temperature near the ice base has limited inter-annual variability, being sourced from the nearby Berkner Bank, the flow speed variations appear to be largely barotropic. As a result, the inter-annual variations at depth are imprinted into the melt rate signal via the melt rate dependency

on flow speed. Highest melt rate years were 1999 and 2018, and in both cases these events followed episodes of anomalously low summer sea-ice concentrations in front of the Ronne Ice Shelf. 2018 was also the highest melt rate year at site R02 and R03 located along the Ronne Depression, nearer the ice front compared with the rest of the sites. However, no sites deeper in the cavity showed an inter-annual maximum in 2018 (Figure 2). This is consistent with an earlier hypothesis of Nicholls and Østerhus (2004) that inter-annual excess of HSSW is routed through the middle of FRIS directly toward Site 5, without first passing around the back of the FRIS cavity past Korff and Henry ice rises (Figure 1). Inter-annual melt rate variability at the back of the FRIS cavity is limited. At R05 located west of Korff Ice Rise, inter-annual variability is expressed as suppression or delay in the arrival of seasonal melt rate minimum. This can be explained by inter-annual stratification changes and different inflow pathways toward the site, respectively.

Melt rates derived in-situ were compared with mean and time-varying estimates from satellite data by Adusumilli et al. (2020). Mean melt rates compare well over Filchner Ice Shelf and the eastern portion of Ronne Ice Shelf. However, the two techniques disagree over the western Ronne Ice Shelf even in their sign and we concluded that the area of active freezing is overestimated in the satellite estimates (Figure 8). In terms of temporal variability, only the Site 5 time series compared relatively well. At the remaining locations the satellite-derived melt rate time series have a strongly exaggerated range of variability at both seasonal and inter-annual time scales and there is no correspondence between their inter-annual variability and that observed in-situ (Figure 9).

We have presented an extensive ApRES melt rate data set from FRIS and shown how these time series can be used to infer variability in the oceanographic environment beneath the ice shelf. We have used these in-situ measurements to identify regions where the reliability of melt rate estimates from satellite data is limited, and therefore melt rates at these key locations should continue to be monitored in-situ. Ultimately, the melt rate time series can serve as a benchmark for assessing the ability of ocean models to represent realistic variability across the ice shelf under present forcing, a necessary condition for accurate projections of melt rate sensitivity to future change of the ice-ocean system.

Data Availability Statement

The ApRES melt rate time series are available at https://doi.org/10.6084/m9.figshare.19783210.v2.

Acknowledgments
This project has received funding from the European Union's Horizon 2020 research and innovation programme under the Marie Skłodowska-Curie grant agreement No 790062. The ApRES data were collected as part of the NERC-funded project NE/L013770/1: Ice shelves in a warming world: Filchner Ice Shelf System (FISS), Antarctica. IV would like to thank Tom Sylvester and Andrew Van Kints for their help retrieving the ApRES data in 2022. The clarity of the paper was significantly improved thanks to the feedback of three anonymous reviewers.

References

Ackley, S. F., Geiger, C. A., King, J. C., Hunke, E. C., & Comiso, J. (2001). The Ronne polynya of 1997/98: Observations of air-ice-ocean interaction. *Annals of Glaciology*, *33*, 425–429. https://doi.org/10.3189/172756401781818725

Adusumilli, S., Fricker, H. A., Medley, B., Padman, L., & Siegfried, M. R. (2020). Interannual variations in meltwater input to the Southern Ocean from Antarctic ice shelves. *Nature Geoscience*, *1*, 616–620. https://doi.org/10.1038/s41561-020-0616-z

Brennan, P. V., Lok, L. B., Nicholls, K., & Corr, H. (2014). Phase-sensitive FMCW radar system for high-precision Antarctic ice shelf profile monitoring. *Sonar Navigation IET Radar*, *8*(7), 776–786. https://doi.org/10.1049/iet-rsn.2013.0053

Bull, C. Y. S., Jenkins, A., Jourdain, N. C., Vaňková, I., Holland, P. R., Mathiot, P., et al. (2021). Remote control of Filchner-Ronne ice shelf melt rates by the Antarctic slope current. *Journal of Geophysical Research: Oceans*, *126*(2). https://doi.org/10.1029/2020JC016550

Daae, K., Hattermann, T., Darelius, E., Mueller, R. D., Naughten, K. A., Timmermann, R., & Hellmer, H. H. (2020). Necessary conditions for warm inflow toward the Filchner ice shelf, Weddell Sea. *Geophysical Research Letters*, *47*(22), e2020GL089237. https://doi.org/10.1029/2020GL089237

Davis, P. E. D., Jenkins, A., Nicholls, K. W., Brennan, P. V., Abrahamsen, E. P., Heywood, K. J., et al. (2018). Variability in basal melting beneath pine Island ice shelf on weekly to monthly timescales. *Journal of Geophysical Research: Oceans*, *123*(11), 8655–8669. https://doi.org/10.1029/2018JC014464

Foldvik, A., Gammelsrød, T., & Tørresen, T. (1985). Circulation and water masses on the southern Weddell Sea shelf. In *Oceanology of the Antarctic continental shelf* (pp. 5–20). American Geophysical Union (AGU). https://doi.org/10.1029/AR043p0005

Gade, H. G. (1979). Melting of ice in sea water: A Primitive model with application to the Antarctic ice shelf and Icebergs. *Journal of Physical Oceanography*, *9*(1), 189–198. https://doi.org/10.1175/1520-0485(1979)009<0189:moiisw>2.0.co;2

Hattermann, T., Nicholls, K. W., Hellmer, H. H., Davis, P. E. D., Janout, M. A., Østerhus, S., et al. (2021). Observed interannual changes beneath Filchner-Ronne Ice Shelf linked to large-scale atmospheric circulation. *Nature Communications*, *12*(1), 2961. https://doi.org/10.1038/s41467-021-23131-x

Hausmann, U., Sallée, J.-B., Jourdain, N. C., Mathiot, P., Rousset, C., Madec, G., et al. (2020). The role of tides in ocean-ice shelf interactions in the Southwestern Weddell Sea. *Journal of Geophysical Research: Oceans*, *125*(6), e2019JC015847. https://doi.org/10.1029/2019JC015847

Hellmer, H. H., Kauker, F., Timmermann, R., Determann, J., & Rae, J. (2012). Twenty-first-century warming of a large Antarctic ice-shelf cavity by a redirected coastal current. *Nature*, *485*(7397), 225–228. https://doi.org/10.1038/nature11064

Hunke, E. C., & Ackley, S. F. (2001). A numerical investigation of the 1997–1998 Ronne Polynya. *Journal of Geophysical Research*, *106*(C10), 22373–22382. https://doi.org/10.1029/2000JC000640

Janout, M. A., Hellmer, H. H., Hattermann, T., Huhn, O., Sültenfuss, J., Østerhus, S., et al. (2021). FRIS Revisited in 2018: On the circulation and water masses at the Filchner and Ronne ice shelves in the southern Weddell Sea. *Journal of Geophysical Research: Oceans*, *126*(6), e2021JC017269. https://doi.org/10.1029/2021JC017269

Jenkins, A., Corr, H. F. J., Nicholls, K. W., Stewart, C. L., & Doake, C. S. M. (2006). Interactions between ice and ocean observed with phase-sensitive radar near an Antarctic ice-shelf grounding line. *Journal of Glaciology*, *52*(178), 325–346. https://doi.org/10.3189/172756506781828502

Jenkins, A., Holland, D. M., Nicholls, K. W., Schröder, M., & Østerhus, S. (2004). Seasonal ventilation of the cavity beneath Filchner-Ronne Ice Shelf simulated with an isopycnic coordinate ocean model. *Journal of Geophysical Research*, *109*(C1), C01024. https://doi.org/10.1029/2001JC001086

Jenkins, A., Nicholls, K. W., & Corr, H. F. J. (2010). Observation and parameterization of ablation at the base of Ronne ice shelf, Antarctica. *Journal of Physical Oceanography*, *40*(10), 2298–2312. https://doi.org/10.1175/2010JPO4317.1

Lambrecht, A., Sandhäger, H., Vaughan, D. G., & Mayer, C. (2007). New ice thickness maps of Filchner–Ronne Ice Shelf, Antarctica, with specific focus on grounding lines and marine ice. *Antarctic Science*, *19*(4), 521–532. https://doi.org/10.1017/S0954102007000661

Lindbäck, K., Moholdt, G., Nicholls, K. W., Hattermann, T., Pratap, B., Thamban, M., & Matsuoka, K. (2019). Spatial and temporal variations in basal melting at Nivlisen ice shelf, East Antarctica, derived from phase-sensitive radars. *The Cryosphere*, *13*, 2579–2595. https://doi.org/10.5194/tc-13-2579-2019

Makinson, K., Schröder, M., & Østerhus, S. (2006). Effect of critical latitude and seasonal stratification on tidal current profiles along Ronne Ice Front, Antarctica. *Journal of Geophysical Research*, *111*(C3). https://doi.org/10.1029/2005JC003062

Naughten, K. A., Jenkins, A., Holland, P. R., Mugford, R. I., Nicholls, K. W., & Munday, D. R. (2019). Modeling the influence of the Weddell polynya on the Filchner–Ronne ice shelf cavity. *Journal of Climate*, *32*(16), 5289–5303. https://doi.org/10.1175/JCLI-D-19-0203.1

Nicholls, K. W. (1996). Temperature variability beneath Ronne ice shelf, Antarctica, from thermistor cables. *Journal of Geophysical Research*, *101*(C1), 1199–1210. https://doi.org/10.1029/95JC02679

Nicholls, K. W. (1997). Predicted reduction in basal melt rates of an Antarctic ice shelf in a warmer climate. *Nature*, *388*(6641), 460–462. https://doi.org/10.1038/41302

Nicholls, K. W. (2018). The study of ice shelf-ocean interaction—Techniques and recent results. *Advances in Polar Science*, *29*(3), 9. https://doi.org/10.13679/j.advps.2018.3.00222

Nicholls, K. W., Corr, H. F., Stewart, C. L., Lok, L. B., Brennan, P. V., & Vaughan, D. G. (2015). A ground-based radar for measuring vertical strain rates and time-varying basal melt rates in ice sheets and shelves. *Journal of Glaciology*, *61*(230), 1079–1087. https://doi.org/10.3189/2015JoG15J073

Nicholls, K. W., & Makinson, K. (1998). Ocean circulation beneath the Western Ronne ice shelf, as derived from in situ measurements of water currents and properties. In *Ocean, ice, and atmosphere: Interactions at the Antarctic continental Margin* (pp. 301–318). American Geophysical Union (AGU). https://doi.org/10.1029/AR075p0301

Nicholls, K. W., Makinson, K., & Johnson, M. R. (1997). New oceanographic data from beneath Ronne ice shelf, Antarctica. *Geophysical Research Letters*, *24*(2), 167–170. https://doi.org/10.1029/96GL03922

Nicholls, K. W., Makinson, K., & Østerhus, S. (2004). Circulation and water masses beneath the northern Ronne ice shelf, Antarctica. *Journal of Geophysical Research*, *109*(C12). https://doi.org/10.1029/2004JC002302

Nicholls, K. W., & Østerhus, S. (2004). Interannual variability and ventilation timescales in the ocean cavity beneath Filchner-Ronne Ice Shelf, Antarctica. *Journal of Geophysical Research*, *109*(C4), C04014. https://doi.org/10.1029/2003JC002149

Nicholls, K. W., Østerhus, S., Makinson, K., Gammelsrød, T., & Fahrbach, E. (2009). ice-ocean processes over the continental shelf of the southern Weddell Sea, Antarctica: A review. *Reviews of Geophysics*, *47*(3), RG3003. https://doi.org/10.1029/2007RG000250

Nicholls, K. W., Østerhus, S., Makinson, K., & Johnson, M. R. (2001). Oceanographic conditions south of Berkner Island, beneath Filchner-Ronne ice shelf, Antarctica. *Journal of Geophysical Research*, *106*(C6), 11481–11492. https://doi.org/10.1029/2000JC000350

Nicholls, K. W., Padman, L., Schröder, M., Woodgate, R. A., Jenkins, A., & Østerhus, S. (2003). Water mass modification over the continental shelf north of Ronne Ice Shelf, Antarctica. *Journal of Geophysical Research*, *108*(C8), 3260. https://doi.org/10.1029/2002JC001713

Padman, L., Fricker, H. A., Coleman, R., Howard, S., & Erofeeva, L. (2002). A new tide model for the Antarctic ice shelves and seas. *Annals of Glaciology*, *34*, 247–254. https://doi.org/10.3189/172756402781817752

Rignot, E., Jacobs, S., Mouginot, J., & Scheuchl, B. (2013). Ice-shelf melting around Antarctica. *Science*, *341*(6143), 266–270. https://doi.org/10.1126/science.1235798

Stewart, C. L. (2018). *Ice-ocean interactions beneath the north-western Ross ice shelf, Antarctica*. Thesis, University of Cambridge. https://doi.org/10.17863/CsAM.21483

Sun, S., Hattermann, T., Pattyn, F., Nicholls, K. W., Drews, R., & Berger, S. (2019). Topographic shelf Waves Control seasonal melting near Antarctic ice shelf grounding lines. *Geophysical Research Letters*, *46*(16), 9824–9832. https://doi.org/10.1029/2019GL083881

Turner, J., Guarino, M. V., Arnatt, J., Jena, B., Marshall, G. J., Phillips, T., et al. (2020). Recent decrease of summer sea ice in the Weddell Sea, Antarctica. *Geophysical Research Letters*, *47*(11), e2020GL087127. https://doi.org/10.1029/2020GL087127

Vaňková, I., Cook, S., Winberry, J. P., Nicholls, K. W., & Galton-Fenzi, B. K. (2021). Deriving melt rates at a complex ice shelf base using in situ radar: Application to Totten ice shelf. *Geophysical Research Letters*, *48*(7). https://doi.org/10.1029/2021GL092692

Vaňková, I., Nicholls, K. W., & Corr, H. F. J. (2021). The nature of ice intermittently accreted at the base of Ronne ice shelf, Antarctica, assessed using phase-sensitive radar. *Journal of Geophysical Research: Oceans*, *126*(10), e2021JC017290. https://doi.org/10.1029/2021JC017290

Vaňková, I., Nicholls, K. W., Corr, H. F. J., Makinson, K., & Brennan, P. V. (2020). Observations of tidal melt and vertical strain at the Filchner-Ronne ice shelf, Antarctica. *Journal of Geophysical Research: Earth Surface*, *125*(1). https://doi.org/10.1029/2019JF005280

Washam, P., Nicholls, K. W., Münchow, A., & Padman, L. (2019). Summer surface melt thins Petermann Gletscher Ice Shelf by enhancing channelized basal melt. *Journal of Glaciology*, *65*, 1–674. https://doi.org/10.1017/jog.2019.43